Design and operation of a superconducting quarter-wave electron gun

J. R. Harris,* K. L. Ferguson, J. W. Lewellen, S. P. Niles, B. Rusnak, R. L. Swent, and W. B. Colson
Physics Department, Naval Postgraduate School, Monterey, California 93943, USA

T. I. Smith
Physics Department, Stanford University, Palo Alto, California 94305, USA

C. H. Boulware and T. L. Grimm
Niowave, Inc., Lansing, Michigan 48906, USA

P. R. Cunningham, M. S. Curtin, D. C. Miccolis, and D. J. Sox
The Boeing Company, West Hills, California 91304, USA

W. S. Graves
Massachusetts Institute of Technology, Cambridge, Massachusetts 02139, USA
(Received 2 December 2010; published 5 May 2011)

Superconducting radio-frequency electron guns are viewed by many as the preferred technology for generating the high-quality, high-current beams needed for future high power free-electron lasers and energy recovery linacs. All previous guns of this type have employed elliptical cavities, but there are potential advantages associated with other geometries. Here we describe the design, commissioning, and initial results from a superconducting radio-frequency electron gun employing a quarter-wave resonator configuration, the first such device to be built and tested. In initial operation, the gun has generated beams with bunch charge in excess of 78 pC, energy of 469 keV, and normalized rms emittances of about 4.9 μm. Currently, bunch charge is limited by the available drive laser energy, and beam energy is limited by x-ray production and the available rf power. No fundamental limits on beam charge or energy have been encountered, and no high-field quenching events have been observed.

DOI: 10.1103/PhysRevSTAB.14.053501 PACS numbers: 29.20.−c

I. INTRODUCTION

The design of an accelerator's beam source and injector plays a major role in determining the maximum current and brightness that can be achieved in that accelerator. As a result, the development of improved electron guns is widely believed to be a key requirement for future high average power free-electron lasers (FELs) and energy recovery linacs (ERLs) [1,2]. Most FELs and ERLs currently employ DC or normal-conducting radio-frequency electron guns. These technologies are highly developed, but impose significant constraints when both high average power and high peak current are required. Superconducting radio-frequency (SRF) electron guns have the potential to improve on both the excellent vacuum qualities of DC guns (generally required for high-quantum-efficiency cathodes), and the high accelerating gradient of normal-conducting radio-frequency guns (needed for high-quality, high-charge beams) [1]. SRF gun technology is currently much less mature than DC and normal-conducting radio-frequency gun technology. This is seen, for example, in the small range of possible SRF gun configurations which have been investigated experimentally. From their initial development [3,4] until now, all SRF guns have employed elliptical cavity geometries, and several guns having this configuration are in operation or development worldwide [5–7]. However, other geometries are possible and may present certain advantages over the standard elliptical type. One such geometry is the quarter-wave resonator, which was developed in the 1980s [8,9] for ion acceleration, and is now in widespread use in that role [10–15]. Quarter-wave resonators use highly reentrant cavities which can be thought of as coaxial transmission lines that are shorted on one end and unterminated on the other end [8]. The longest resonant wavelength in these structures is about 4 times the cavity length. In practice, the operating frequency will be altered somewhat by tapering of the center conductor, capacitive loading at the unterminated end, and similar effects. When modified for use as electron guns, quarter-wave resonators offer a number of advantages which flow from their small size and ability to operate at relatively low frequencies [6,7,16]. Because they rely on highly reentrant geometries, the time of flight of electrons across the

*Corresponding author.
jrharris@nps.edu.

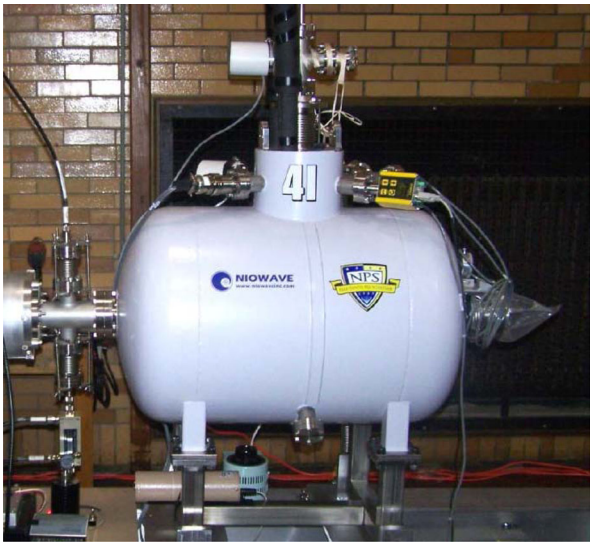

FIG. 1. The 500 MHz quarter-wave SRF gun. This photograph was taken before insertion of the cathode stalk and application of lead sheet radiation shielding. Note the power coupler connections to the left of the cavity.

accelerating gap can be made to be a small fraction of an rf period. For the picosecond-class beams typically used in FELs, this will cause the gap voltage to be effectively constant during the beam's passage. Alternatively, the long rf wavelength allows for the use of longer beams when reduced peak current is desired to minimize space charge effects. Other potential advantages include the reduced cost associated with lower-frequency rf sources, the ability to operate at 4.2 K with compact cavities, reduced rf losses on the cathode, and flexibility in how cathodes can be mounted in the gun. Because of these potential benefits, quarter-wave SRF electron gun projects have been initiated by the Naval Postgraduate School (NPS), the University of Wisconsin, and Brookhaven National Laboratory; all of these projects are being pursued in conjunction with Niowave, Inc. [6].

We previously reported first operation of the NPS SRF gun (Fig. 1) in Ref. [17]. This prototype is the first SRF gun to be based on the quarter-wave resonator geometry, and went from initial concept to first beam in under two years. Here we present details of the design, commissioning, and initial performance of this gun. In initial testing, the gun was able to produce beams with energy of (469 ± 22) keV, bunch charge in excess of 78 pC, and a typical normalized rms emittance of 4.9 μm (Table I). Beam energy has been limited by the available rf power and radiation shielding, and no high-field quenching events have been observed.

TABLE I. Gun parameters.

Parameter	Objective	Demonstrated
Resonant frequency	500 MHz	501 MHz
Operating temperature	4.2 K	4.2 K and below[a]
Residual resistance	5 nΩ	···
BCS resistance	99 nΩ	···
P_{wall}	9.5 W	···
Quality factor (cavity)	1.2×10^{9}[b]	0.8×10^{9}[a,c]
Quality factor (gun)	···	5×10^{7} typical[a,d]
Geometry factor	126 Ω	···
R/Q	195 Ω	···
Beam energy	1.2 MeV	469 ± 22 keV[e]
Electric field on cathode	29 MV/m	···
Peak electric field	51 MV/m	···
Peak magnetic field	78 mT	···
Transit time factor	0.96	···
Cathode QE	···	$1–2 \times 10^{-6}$
Bunch charge	1 nC	78 pC[f]
Emittance (rms normalized)	<10 μm	4.9 μm typ.[g]

[a]See Table II and Fig. 13.
[b]Calculated without including cathode stalk or power coupler.
[c]Measured without including cathode stalk.
[d]Measured with cathode stalk installed.
[e]Limited by radiation shielding and rf power in current facility.
[f]Limited by laser energy and cathode QE.
[g]See Table IV.

II. DESIGN AND ASSEMBLY

A. Project concept

NPS recently established an experimental accelerator and FEL physics program as an outgrowth of its long-standing FEL theory group. This program was intended to utilize the components of the Stanford Superconducting Accelerator (SCA), to be reassembled in a new configuration in a new facility at NPS [16,18,19]. While the SCA used nine-cell TESLA-type speed of light structures, its DC electron gun was limited to about 230 keV, which resulted in significant phase slip in the first accelerating structure. For the new installation at NPS, it was decided to add a booster cell after the gun to correct this, and a quarter-wave SRF structure was selected for the reasons discussed above. An operating frequency of 500 MHz was chosen because it allows for a structure of reasonable size and a beam injection rate of 100 MHz into the 1.3 GHz SCA linac structures. At this rate, a bunch charge of 10 pC would give an average current of 1 mA. It was soon realized that, by adding a removable cathode stalk, the cavity could be converted into a gun while retaining the ability to later operate as a booster, and the gun configuration became the focus of the project. The design objective for the cavity when operating as a gun was generation of a 1 nC bunch accelerated to 1.2 MeV. Rather than trying to build a fully optimized gun/booster design, it was decided to rapidly field a prototype employing a simplified design. This approach enabled us to move from initial concept to first rf testing in less than one year, and from initial concept to first beam in less than two years. It should also allow us to find "unknown unknowns" and leverage operational experience into an improved follow-up design. However, this approach required that some components

desired in a final system, like rf tuners, be eliminated from the prototype design. Some of the design tradeoffs associated with this approach will be detailed below.

B. Cavity and cryostat

Figure 2 shows a cross section of the cavity and cryostat in booster configuration, without the cathode stalk installed. The end plates and ''nose cone'' or center conductor were machined from large-grain niobium ingots with a residual resistivity ratio (RRR) of about 180. The sidewalls were formed from fine-grain (ASTM 5) rolled niobium with a RRR of about 300. Bead-pull and mode spectrum measurements were performed before final cavity assembly, which was accomplished by electron beam welding. The joints connecting the end plates and sidewalls in this simplified design do not have the rounded internal corners which are generally desired for ease of cleaning and to mitigate multipacting; rounded internal corners are included in the second-generation SRF quarter-wave guns now under development for Wisconsin and Brookhaven [6]. After final assembly, the cavity underwent buffered chemical polish (BCP) etching using two parts phosphoric acid (H_3PO_4), one part nitric acid (HNO_3), and one part hydrofluoric acid (HF). This removed approximately 150 μm of material, and was followed by a high-pressure rinse with ultrapure water. The cavity was brazed to stainless steel flanges on either end, bolted to stainless steel pipe, and then surrounded by a stainless steel liquid helium vessel to provide 6.8 L of liquid helium reservoir capacity. System temperature and helium level sensing are accomplished by nine silicon diode temperature sensors located throughout the cryostat, and by a 1/8 W, 100 Ω (at 300 K) carbon resistor which has a large, known variation of resistance with temperature. A NbTi solenoid is located downstream of the cavity for focusing and emittance compensation. This solenoid has an iron yoke to provide a flux-return path and to localize the magnetic field, and is attached to the liquid helium vessel with two copper bars. Although intended to be superconducting, there is insufficient heat transfer through these bars to keep the solenoid below its critical temperature of approximately 9 K [20]. The liquid helium vessel and solenoid are surrounded by a liquid nitrogen shield and multilayer insulation, which are in turn surrounded by a mu-metal magnetic shield and a low-carbon steel vacuum vessel. The regions between these layers are held at vacuum.

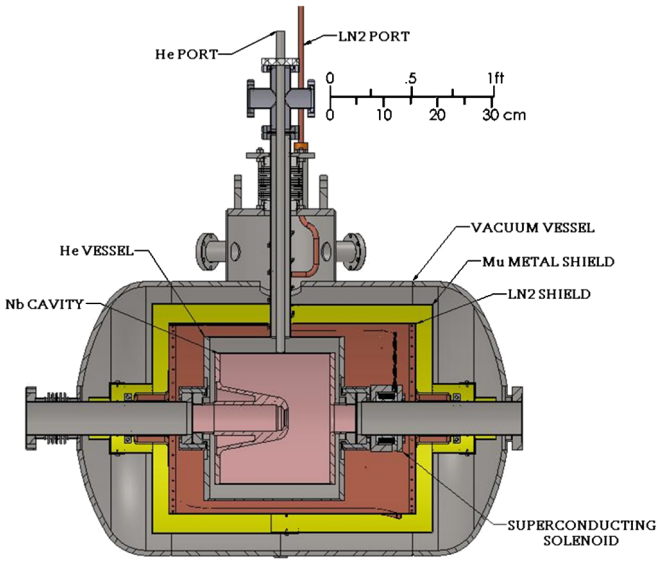

FIG. 2. Cross section of the cavity without the cathode stalk or coupler installed.

C. Cathode and cathode stalk

The development of advanced, high-quantum-efficiency photocathodes compatible with operation in SRF guns is considered to be a key area of research for high average power FELs and ERLs [1,6]. Unfortunately, many of the advanced photocathodes currently under development require dedicated preparation and load-lock systems which were not compatible with this project's objective of rapid construction and testing of a simplified prototype. Contamination of the cavity by the cathode during operation is also of concern [21,22]. As a result, we chose to use fine-grain normal-conducting niobium as the cathode material for our initial testing. By using niobium, it was hoped that any material sputtered off the cathode and deposited into the cavity would have a minimal effect on overall cavity operation. This cathode consisted of a niobium button etched with buffered chemical polish in the same manner as the cavity, and press fit into the cathode stalk (Fig. 3). The simplicity of this attachment method allows

FIG. 3. Niobium cathode. The machined holes and slots on each side of the cathode allow insertion of a tool used to press the cathode into the cathode stalk, and allow the cathode base to flex for a tight fit during insertion. In this way, the cathode can be inserted without risking damage to its emitting surface.

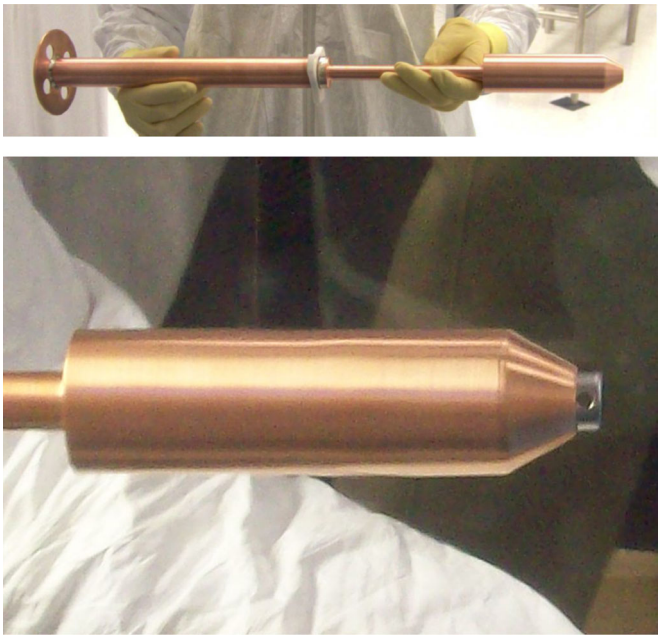

FIG. 4. Top: cathode stalk without an installed cathode. Bottom: detail of installed cathode.

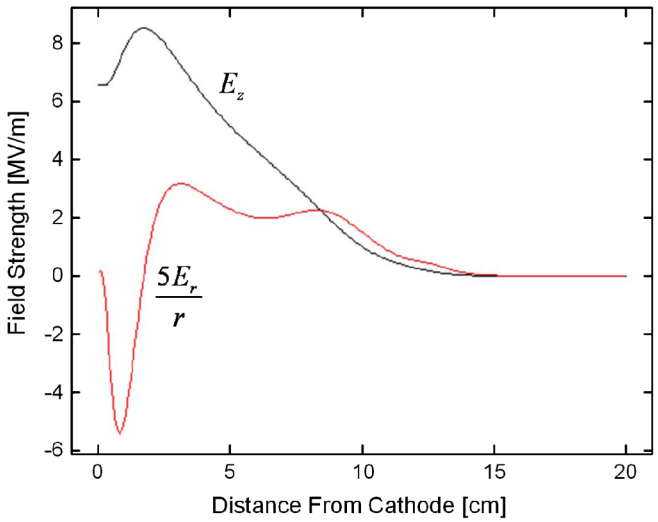

FIG. 6. Simulated longitudinal and radial electric fields along the gun axis, corresponding to a beam with energy 480 keV and launch phase of 40 degrees.

for testing of other cathode materials and configurations in the future, and initial simulation studies of field emitter operation in the gun have already begun [23]. Figure 4 shows a photograph of the cathode and cathode stalk assembly, and Fig. 5 shows a drawing of the cathode stalk inserted into the cavity. The stalk is normal conducting, and made of copper. It has no direct physical contact with the cold cavity, which reduces both the heat flow into the cavity and the possibility of generating particulate contamination, but allows some rf power to flow out of the cavity. This design also avoids the use of a choke cavity filter, which can make cleaning difficult and lead to excess field emission [6]. The stalk is nonresonant at the cavity fundamental frequency. Its length was optimized for minimum rf power dissipation at that frequency, and it has transitions in radius to provide impedance mismatches for minimizing rf power flow into the normal-conducting region. Two capacitively coupled antennas are present in this region to sense the power on the stalk, or to inject an rf signal to disrupt multipacting. This region is held under vacuum by a dedicated vacuum pump. Mechanically, the cathode stalk is cantilevered, with a Teflon ''spider'' placed at the location of expected minimum field to center the stalk inside the pipe. The cathode stalk is attached to a mounting plate, which in turn is attached to the outer pipe and cryostat by bellows. A mounting fixture and series of screws hold the bellows in position, and allow for adjusting the stalk's pitch, yaw, and axial location. This arrangement allows the cathode to be moved from a fully retracted location 14 mm inside the niobium nose cone to a fully inserted location 1.5 mm inside the cavity; these values are not corrected for shrinkage at cryogenic temperatures. This adjustment alters the transverse focusing and axial accelerating fields at the cathode tip, and changes the power coupling into the stalk region; typical values for the longitudinal and axial electric fields are shown in Fig. 6. Simulations indicate that when the cathode is retracted

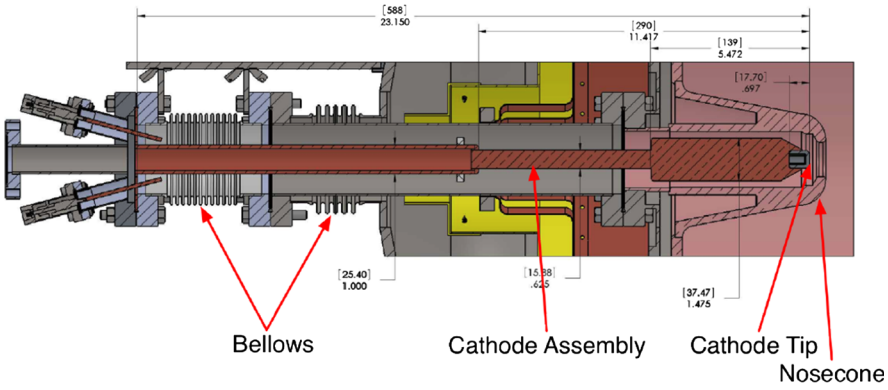

FIG. 5. Detail of cathode stalk from rear shorting plate to cavity.

into the nose cone by 6.5 mm, an accelerating field of 17 MV/m will be present on the cathode when the cavity is at full power; this accelerating field is sufficient for activating diamond field emitter arrays [24].

D. Power coupler and rf system

Initial testing was performed using a cascaded rf power coupler system, shown in Fig. 7. The primary stage is a coaxial coupler, which serves to minimize dipole kicks to the beam and provides for higher order mode extraction. The outer conductor is a stainless steel tube attached to the cryostat and cavity, and the inner conductor is a copper tube. This copper tube is articulated in a manner similar to the cathode stalk, and can be moved axially to increase or decrease coupling into the cavity. Electrons accelerated from the gun are directed through the center of the copper tube. The secondary stage of the coupler is formed by a pair of capacitively coupled antennas like those used on the cathode stalk, which couple rf energy into and out of the coaxial coupler. One of these antennas is driven, and forward and reflected power are measured at that location. The second antenna is used to measure the transmitted power flowing out of the cavity. This is evident from the photograph in Fig. 1, taken during initial cavity testing, where the forward and reflected power are measured at the lower antenna (note the directional coupler) and the transmitted power is measured at the upper antenna. Interference from direct coupling of the two antennas contributes error to the measurement of the cavity fields. Based on measurements of this coupling when the cavity was at room temperature, we estimate the error in field level determination to be 10% or less. An improved power coupler design more suited to high power operation is currently being developed.

A schematic of the typical rf drive system used in these experiments is shown in Fig. 8. A reference oscillator nominally at 83.3 MHz serves as the master clock. This provides a timing signal to the UV drive laser and is the source for a frequency multiplier providing a 500 MHz input to the solid state amplifier. The currently installed amplifier is capable of delivering 100 W forward power to the cavity. A circulator sends reflected power to a dummy load. The phase detection circuit takes as input the multiplied reference waveform and the signal from a pickup probe, generating an error signal to the voltage-controlled oscillator input on the reference source. A variable attenuator before the amplifier allows control over the input power to the cavity, while power for the laser timing and the reference arm of the phase detection circuit is

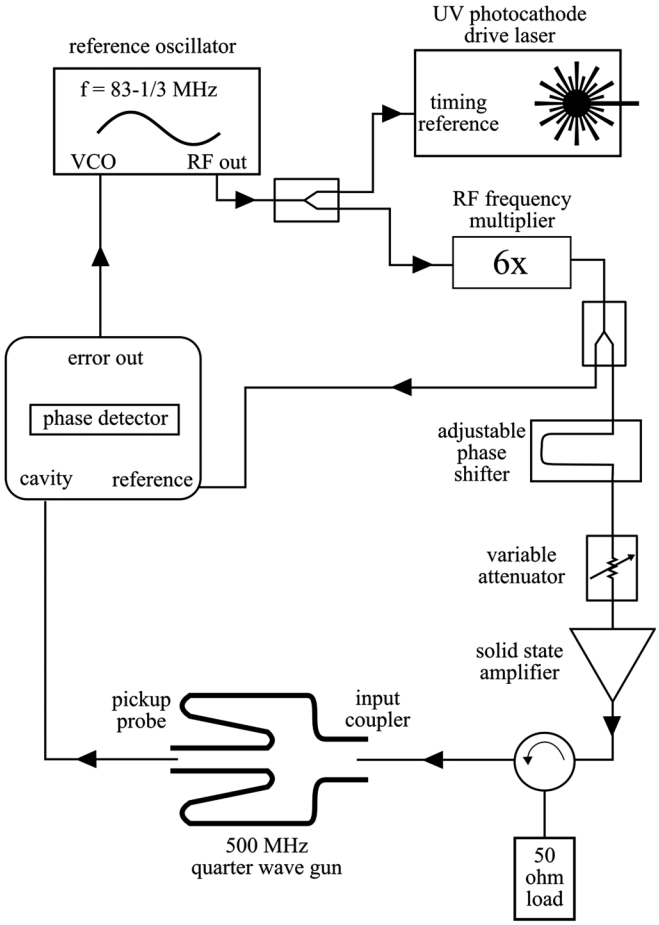

FIG. 8. Schematic of the rf control circuit, including timing reference for the photocathode laser, variable forward power control, and phase delay. Forward and reflected power are measured at the input coupler and transmitted power at the pickup probe.

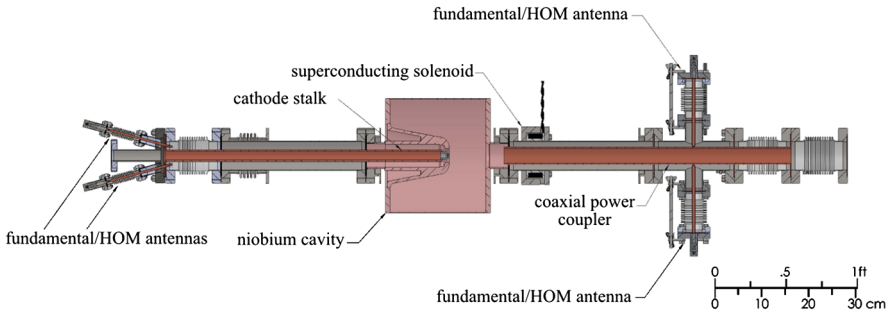

FIG. 7. Cathode stalk, cavity, and power coupler. The cathode stalk shown here was an earlier design before discontinuities were introduced to reduce rf power flow.

constant. The phase lock of both the UV laser timing and the rf input is therefore able to accommodate large changes in the cavity fields, with the nominal relative phase delay between the laser pulse and the rf drive constantly monitored using the output of a UV photodiode in the optical train.

E. Laser system

Photoelectrons were produced using a modified Coherent Elite DUO laser generating 266 nm light at a nominal energy of 1 mJ per pulse. This system was designed to serve a dual role as a photocathode drive laser for this electron gun, and for use in laser damage studies by Boeing. The system is based on a mode-locked Ti:sapphire seed laser, producing 18 fs-long pulses at a repetition rate of 1 kHz. A Pockels cell is used to select pulses for injection into the amplifier stages, which are pumped by doubled yttrium aluminum garnet (YAG) lasers. Amplified pulse lengths can be adjusted between 10 and 38 ps with a pulse stretcher, and exhibit a low-order super-Gaussian transverse profile with several higher intensity regions. This structure is very stable, and the shot-to-shot UV energy variation is typically about 3%. Laser energy is easily and reproducibly adjusted by rotating half-wave plates in the optical beam line. The maximum laser beam diameter at the cathode is 10 mm, and can be adjusted by the use of plates with 1 or 5 mm apertures, which are inserted into the laser path and imaged onto the cathode. The laser is transported from the laser room to a final optics station adjacent to the gun. At this station, a very small fraction ($\ll 1\%$) of the beam is split into a diagnostics path and directed onto the ''virtual cathode,'' while the primary beam is directed through a vacuum window, and then onto the cathode by a one-square-inch aluminized fused silica mirror inside the beam line laser cross. For calibration purposes, the laser energy can be measured just before passage through the vacuum window, with 18% of the laser energy subsequently lost at the window and in-vacuum mirror.

F. Diagnostic beam line and controls

Measurement of electron beam properties is accomplished with the diagnostic beam line shown in Fig. 9. Immediately downstream of the laser mirror are two diagnostics stations. Each station has a movable, motor-driven diagnostics module consisting of a one-inch diameter, 0.5 mm thick cerium-doped YAG crystal and mirror for observation of the beam size and transverse distribution, and a metal plate for measuring beam charge or for placement of slits for emittance measurements (Fig. 10). To enable charge measurements, the diagnostics modules and drive motor assemblies are electrically isolated from the beam line by a glass break. The motors for these modules are remotely controlled using a LABVIEW program. Basler A102f CCD cameras mounted above the beam line enable viewing the YAG screen through UV-opaque windows, with camera control and image acquisition provided by an independent LABVIEW program. These diagnostics stations are followed by a nonintercepting capacitive bunch charge detector and a normal-conducting solenoid.

Just downstream of the beam line solenoid is the first of several capacitive beam position monitors (BPMs). The BPMs use button electrodes and an electronics module designed for fast processing of beam position signals. This log-ratio BPM derives beam position from the logarithm of the ratio of opposite pickup signals [$\log(A/B)$]. Position measured by this method is more linear, over a wider range, than position measured by the difference-over-sum technique. Input signals are processed in parallel, allowing a single-pass position measurement.

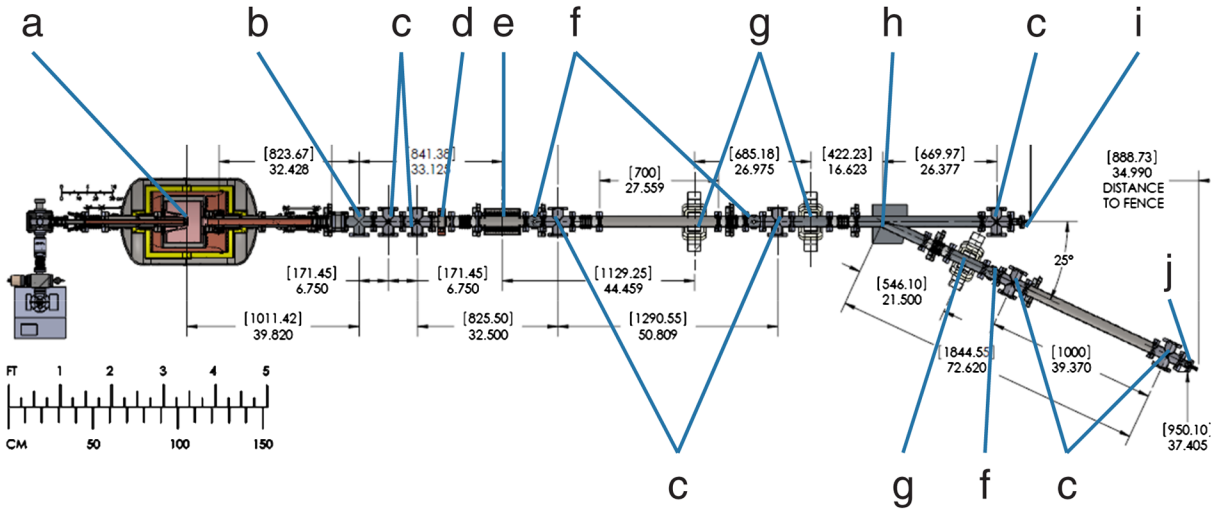

FIG. 9. Diagnostic beam line, showing (a) cavity, (b) laser cross, (c) diagnostics stations, (d) capacitive beam pickup, (e) solenoid, (f) BPMs, (g) quadrupole magnets, (h) dipole magnet, (i) end-of-line UV-transmissive window, and (j) fast Faraday cup.

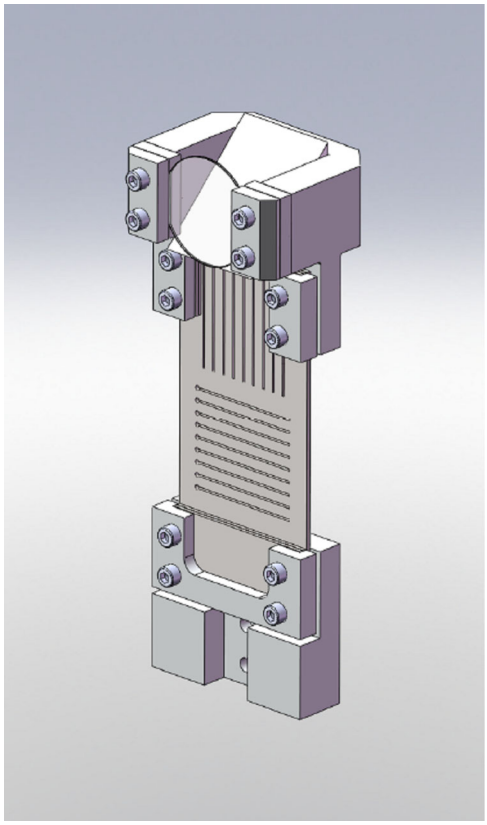

FIG. 10. Diagnostics module, showing circular YAG screen and mirror for viewing the beam transverse profile, and slits for emittance measurements. The slit plate is replaceable with blank plates for charge measurements, or with pinhole aperture plates.

The first BPM is followed in the beam line by another diagnostic station, a quadrupole magnet, another BPM and diagnostics station, a second quadrupole magnet, and a dipole magnet. The dipole magnet allows the beam to be deflected 25° into a spectrometer line having another quadrupole magnet, BPM, pair of diagnostics stations, and a fast Faraday cup. This branch of the transport line is intended for measurement of the beam energy and energy spread. The undeflected path has a final diagnostics station and was originally intended to end in a fast Faraday cup. This cup was replaced by a UV-transmissive window to enable direct observation of the cathode with a visible-light telescope or a UV-sensitive JAI CM-140GE-UV CCD UV camera equipped with a 105 mm lens. This allows laser spot location and alignment to be directly verified (Fig. 11). Window-frame corrector magnets are distributed at various points along the beam line, generally just upstream of diagnostics stations, to facilitate beam steering and transport through the system. In the present configuration, corrector magnets are controlled by independent manual power supplies while the NbTi solenoid, beam line solenoid, quadrupole magnets, and the dipole are controlled remotely using a third independent LABVIEW program. We plan to merge the various LABVIEW programs into a single EPICS-based control environment before testing resumes.

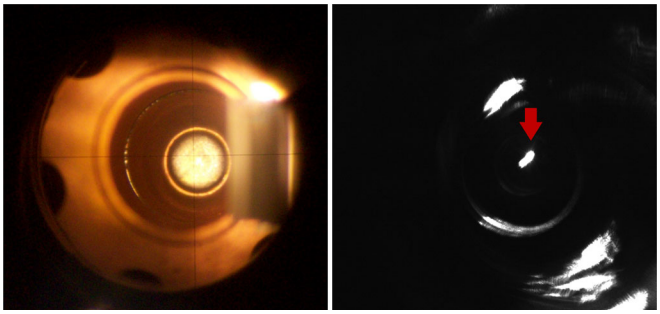

FIG. 11. Visible light and UV images of the cathode, taken through the end-of-line window. The cathode appears off center due to misalignment of the tripod supporting the telescope. The blurred square object in the visible light image is the in-vacuum laser mirror. The UV image shows the location of the drive laser on the niobium cathode, indicated by the red arrow.

Because of the inability to cool the NbTi solenoid to superconducting temperature, it must be pulsed to prevent excessive heating of the cryostat. The rise and fall times of the solenoid in turn limit the beam repetition rate to 1 Hz or below. The solenoid must be turned on several hundred milliseconds before the laser arrives at the cathode to allow the field to stabilize, and the CCD cameras also need an advance trigger to allow them to complete their setup before the laser pulse arrives. To accomplish this, the Pockels cell located between the seed laser and the first amplifier stage is continually run at 1 Hz, controlled by a master trigger signal from a DG 535 trigger generator. This master trigger signal is also sent to a second trigger generator, which is used to generate delayed trigger pulses for the solenoid and cameras. The solenoid is turned on about 800 ms after arrival of the master trigger so the field will be stable for the following pulse. The CCD cameras require about 60 μs of setup time so they are given a trigger pulse that is delayed by approximately 940 ms from the master trigger. The integration time on the CCD cameras is set to their minimum value of 20 μs, giving clean images of the beam with little background. The integration time is still much longer than the YAG fluorescence time of roughly 100 ns, so the cameras will collect all the fluorescence light as long as the laser pulse is timed to strike the cathode somewhere near the middle of the integration window.

III. COMMISSIONING AND INITIAL RESULTS

A. Cavity tests

Cryogenic testing consisted of two phases: (1) cavity operation without the cathode stalk, and (2) cathode stalk insertion and operation as an electron gun. Two sets of cavity tests were performed, with the first set occurring in September 2009. This test, along with all other experiments reported here, was conducted at the Niowave facility

in Lansing, MI. Prior to applying rf to the cavity, its vacuum was at 10^{-8} Torr, and no initial bakeout was performed. The cavity was cooled to 4.2 K over a period of about two hours, with a measured frequency shift from 500.3 MHz at room temperature to 501.0 MHz at cryogenic temperature. The static heat load was measured to be about 1.5 W, corresponding to a helium use rate of 2.1 L/hr. This required a refill of the reservoir every two hours. Power was then applied to the cavity. The coupling coefficient β was determined from measurements of the incident and reflected power, while the cavity Q was calculated from the decay of the cavity fields when the rf power was turned off. The cavity Q was plotted against the calculated integrated cavity voltage, and is shown in Fig. 12. This test was limited by x-ray radiation produced by accelerated field-emitted electrons. During the tests described in this paper, the Niowave facility did not have permanently installed radiation shielding, which imposed limits on how much power could be applied to the gun.

The second set of cavity tests occurred in October 2009. Helium processing [25,26] was employed, which approximately tripled the achieved fields. The highest fields during this test corresponded to an accelerating voltage of 760 kV, although no Q measurement was performed at this operating point. The cavity field strength was limited by the x-ray flux and the available rf power; at no time was the cavity seen to quench when there was sufficient liquid helium in the cavity reservoir. The bifurcated curve in Fig. 12 is due to the cavity running out of helium and the test being repeated after refilling the reservoir. While the cavity was primarily operated at 4.2 K, lower-temperature operation was tested by using a roughing pump to lower the pressure in the liquid helium reservoir, resulting in a significant improvement in Q (Fig. 13). Fundamental and higher order mode frequencies were generally in very good agreement with predictions made using SUPERFISH. The five lowest predicted modes were all observed in the experiment, with the measured frequencies differing from the predicted values by less than 1.2%. Two additional modes, believed to be nonaxisymmetric TE modes, were observed experimentally that were not seen in SUPERFISH.

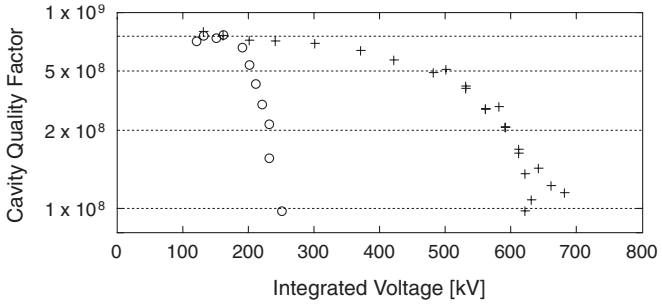

FIG. 12. Cavity Q during testing in September 2009 (circles) and October 2009 (crosses).

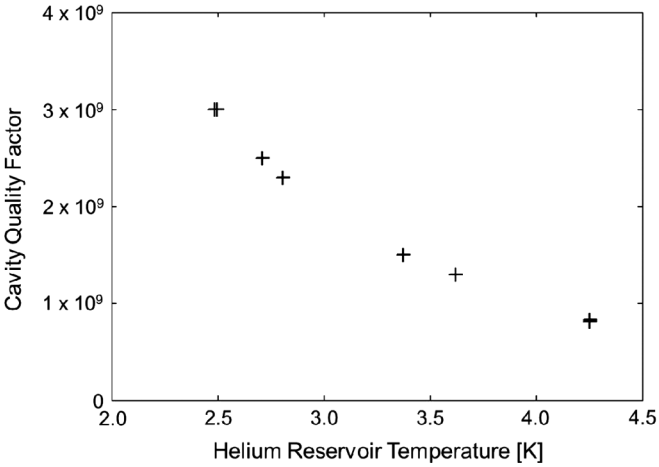

FIG. 13. Effect on cavity Q due to operation at reduced temperature. Temperature was determined by measuring the pressure of the helium vapor during vacuum pumping on the reservoir, and applying the fitting curve $P(T) = \exp[(\frac{T-1.53}{0.01467})^{0.3704}]$ relating the liquid helium vapor pressure P and liquid temperature T. This fit agrees with previously reported experimental data to within $\pm 3\%$ for temperatures above 1.6 K [33].

B. Cathode insertion and operation as an electron gun

1. General performance

Final assembly of the gun occurred on 10 May 2010 with insertion of the cathode stalk. Initial rf testing with the installed cathode was performed on 8 June 2010, and first beam was achieved shortly after 11:10 AM the following day. By the end of that day the beam had been successfully transported to the end of the beam line and down the spectrometer line. Six days of additional experiments occurred during June and July. Our overall impression has been that the system is quite reliable, even under continual operation. Radiation continued to place constraints on our operations, despite the addition of local lead shielding around the cavity. When bringing up rf power with the cathode installed, multipacting barriers were present but were overcome in short order. We have not needed to try rf injection into the cathode stalk to disrupt multipacting. While others have reported detection by CCD cameras of anomalous light-emitting phenomena in operating SRF cavities [27], no evidence of such effects has been seen with the UV camera at the end-of-line station. It is possible that this is simply due to the very limited field of view available at that station.

Beam properties seem to be insensitive to cavity temperature when it is below about 6 K, as indicated by the temperature sensor at the top of the cavity. When this temperature approaches 7 K, the beam shape seen on YAG screens becomes distorted. This distortion served as a useful indication to the operators that the cavity was about to return to its normal-conducting state. In our first tests, the cavity reservoir would be filled, and testing would

continue until enough helium had evaporated that part of the cavity was no longer superconducting. During typical operation at 10 W forward power, each fill of the cryostat lasted about 30 minutes, for a helium use rate of about 14 L/hr. To increase the operational availability of the gun and improve stability, we shifted to quasicontinuous flow of liquid helium into the reservoir. In this mode, an operator monitors the cavity temperature while watching the helium exhaust plume emitted from the gun. Liquid helium is intermittently pushed into the gun reservoir in quantities sufficient to keep the cavity temperature constant but not to overfill the cryostat reservoir. Cavity temperature is typically maintained at around 5 K during operation. Overall helium consumption rates during the most recent runs averaged about 250 L per day, including overnight periods when the cavity was not operated, but was kept cold enough to avoid Q disease [28]. This consumption rate is significantly higher than during the cavity tests in 2009 due to additional heating from the cathode stalk and NbTi solenoid operation. When operated at a 1 Hz repetition rate, heating of the solenoid increases its resistance, limiting its current to about 1.1 A with the power supply which is presently installed. Currents up to 4 A can be achieved in single-pulse operation.

While dark current is very noticeable at the first YAG screen, attempts to measure it using a 50 Ω termination and oscilloscope have not been successful. This suggests that less than 20 μA of dark current is being intercepted by the first YAG screen. While this dark current is much smaller than the peak photoelectron beam current (typically 5 A), it most likely constitutes the majority of the charge leaving the gun. A darkening of the mirror for the first YAG screen has been observed, possibly due to dark current interception. Adjusting the solenoid to focus the photoemission beam on the first YAG screen is seen to deflect the vast majority of the dark current off that YAG screen. This indicates that the primary source of dark current is not on the cathode, and is consistent with simulations showing that the region of highest electric field is located on the nose cone (Fig. 14).

Alignment of the cathode, the cavity electromagnetic axis, and the NbTi solenoid magnetic axis appears to be good. A position for the laser spot can be found near the cathode center such that changing the solenoid current yields little deflection of the photoemission beam. The electron beam at the first YAG screen replicates the transverse shape of the laser beam for 5 and 1 mm spot sizes, indicating that all of the beam is being transported out of the gun and that the electron optics in the cavity are reasonably good.

Cavity Q was reduced by the presence of the cathode, and varied as a function of cathode location, as summarized in Table II. Adjusting the cathode stalk position is simple and repeatable due to the screw mechanism used to position it. In general, moving the cathode requires a corresponding change in coupler position to maintain unity coupling. Beam tests have been performed at 8 mm retraction and 10 mm retraction. The reflected power was small in each location, and so no change was made in the coupler position when shifting between these locations. This change shifted the resonant frequency from 500.981 MHz at 10 mm retraction to 500.956 MHz at 8 mm retraction.

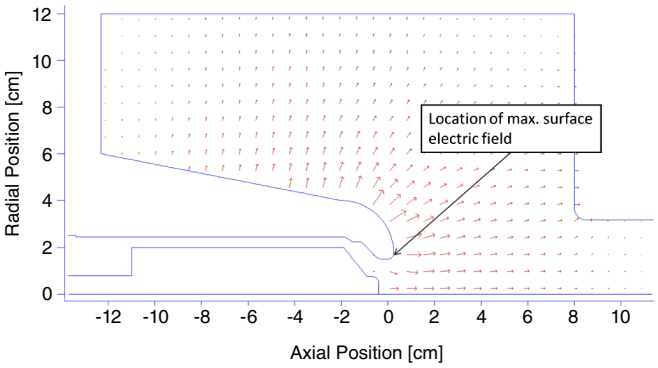

FIG. 14. Location of peak surface electric field in the cavity. With the cathode recessed 6.5 mm inside the nose cone, an on-cathode gradient of 6.5 MV/m at a phase of 90 degrees corresponds to a field on the tip of the nose cone of approximately 17.4 MV/m.

Several anomalous effects have been observed but not yet fully explained. There are some indications that we may be charging the laser mirror, resulting in intermittent deflection of the electron beam but no observable damage to the mirror. Some apparent discharges in the cathode stalk region have been observed, evidenced by increased beam current and vacuum excursions, but there appears to be no adverse impact on system operation. Some apparent discharge events have also been observed on the diagnostics modules, possibly due to charging by dark current.

2. Quantum efficiency

A large number of measurements of bunch charge as a function of laser energy were made under various operating conditions. No significant evidence of saturation was seen in any data set, indicating that we have not yet reached

TABLE II. Cavity quality factor.

Cathode location [mm]	Operating pressure [Torr]	Quality factor
Not installed[a]	82	3×10^9
Not installed	760	8×10^8
−14	760	5×10^8
−9	760	$3–6 \times 10^7$
−6	760	2×10^7

[a]Extreme value obtained during reduced-pressure operation. See Fig. 13 for more data.

the maximum charge that can be extracted from this gun.[1] The quantum efficiency (QE) observed with the niobium cathode used in these experiments consistently fell in the range $1–2 \times 10^{-6}$. This agrees well with the value of 2×10^{-6} obtained in a preliminary 5 kV DC test stand experiment using a niobium button cathode made from the same type of material, and prepared in an identical way to the actual cathode. A quantum efficiency of 2×10^{-6} was also reported by Brookhaven from measurements in an SRF cavity using a 266 nm laser, but this measurement occurred after laser cleaning of the emitting surface [29]. Without laser cleaning, their BCP-polished niobium photocathodes exhibited quantum efficiencies of about 10^{-7} [30]. However, the laser energy density in our experiments was about 100 times less than that required for laser cleaning of niobium cathodes [30]. The discrepancy between our results and those reported in the literature is not understood at this time. To date, there is no clear indication of degradation in the quantum efficiency of the cathode, and no damage to the cathode has been observed.

3. Beam charge and rf power

Figure 15 shows the beam charge measured at the first diagnostics station as a function of calculated integrated cavity voltage determined from measurements of the transmitted rf power. The cathode was illuminated with a 5 mm laser spot, with the laser adjusted to provide energies of 169 μJ, 154 μJ, or 94 μJ to the cathode. All measurements were taken on the same day, with the cathode 10 mm inside the nose cone. Error bars were determined for high laser power operation by observing the shot-to-shot variation in measured beam current.

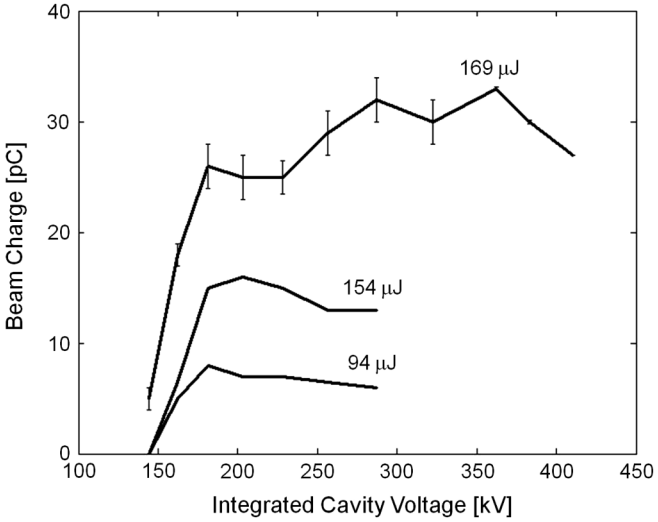

FIG. 15. Beam charge measured at the first diagnostics station, for three levels of cathode illumination, as a function of integrated cavity voltage calculated from measurements of the transmitted rf power.

4. Phase scan (cathode location and illumination)

As with all rf guns, the extracted current depends in part on the arrival time of the laser at the cathode with respect to the phase of the rf field in the gun. However, the range of arrival phases over which beam can be extracted is influenced by other system parameters, including beam energy and cathode location. Figure 16 is one example of the many phase scans performed. It shows the extracted beam charge measured at the second diagnostics station as a function of the laser arrival within the rf cycle, measured in degrees past the rf zero crossing. In this case, the laser timing remained fixed while a variable delay was introduced into the transmission line delivering rf to the cavity. Significant bunch charge could be extracted between about 15 and 90 degrees, with the peak current occurring at the larger phase; these results are typical of the other measurements performed. Measurements were performed with the cathode at 10 mm retraction (red) and 8 mm retraction (black). The data taken at 10 mm retraction was with a laser energy of 170 μJ, while the data taken at 8 mm retraction used laser energies of 155 μJ (solid) and 79.8 μJ (dot). This data indicates that moving the cathode from 8 to 10 mm reduced the range of launch phases over which beam could be extracted from the gun.

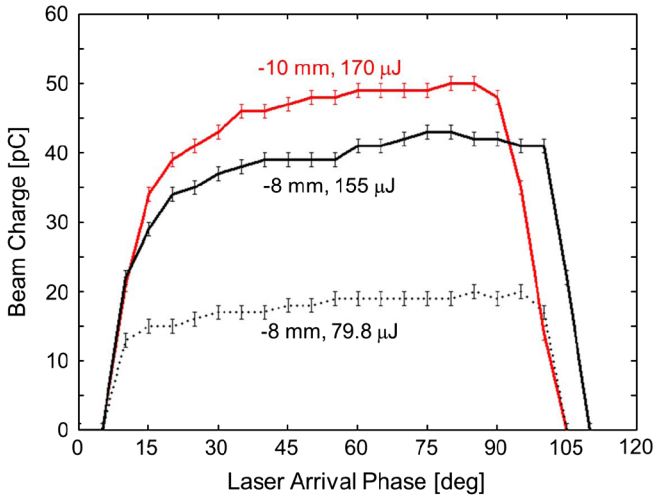

FIG. 16. Beam charge measured at the second diagnostics station as a function of laser arrival phase for the cathode at 10 mm retraction (red) and 8 mm retraction (black). The data taken at 10 mm retraction was with a laser energy of 170 μJ, while the data taken at 8 mm retraction used laser energies of 155 μJ (solid) and 79.8 μJ (dot).

[1]The typical peak surface electric field on the cathode tip in these experiments is estimated at 6.5 MV/m. For a launch phase of 45 degrees, and a laser spot radius of 2.5 mm, the emission limit predicted by Gauss' law is 0.8 nC.

5. Beam energy and cavity integrated voltage

Four experiments were conducted using the dipole and spectrometer line to investigate the dependence of beam energy on cavity rf power, and the results of these experiments are summarized in Table III and Fig. 17. Prior to each set of tests, the beam was aligned to the center of the dipole using YAG screens upstream and downstream of the dipole. The dipole was then powered, and as the cavity power was changed, the dipole current was adjusted to keep the beam on the center of the YAG screen in the spectrometer line. The alignment process was generally not repeated during each series of measurements. However, several measurements during experiment 2 were repeated, with the beam realigned before each measurement. These data points are indicated as experiment 2A. Most of the data falls along the trend line indicated in Fig. 17. Experiment 4 was complicated by the failure of one of the YAG screen drive motors, requiring alignment over a longer distance. Half of the data in experiment 2 falls along the primary trend line, with the remainder falling along a different line with a similar slope. The cause of this is unknown, but would appear to be due to some unnoticed, discrete event that occurred during the test sequence, and may be related to the apparent charging and discharging of the laser mirror and the resulting observed beam deflection. This deflection could cause the beam to become misaligned through the dipole, thereby altering the dipole current needed to center the beam on the spectrometer line YAG screens, which would be perceived as a change in beam energy. In the log book, no record of this type of event was made during this run. However, the magnitude and direction of the change in the measured energies are consistent with the magnitude and direction of a change in measured beam energy observed during such a discharging event which occurred in a different test sequence. As expected, the laser energy (and therefore the extracted charge) had no noticeable effect on the beam energy. Shifting the cathode location by 2 mm also seems to have had no significant effect on the beam energy.

A comparison of the experimental data shown in Fig. 17 with preliminary simulations of the gun suggests that the actual integrated cavity voltage is less than the calculated integrated cavity voltage associated with the fundamental by about 85 kV, although the source of this possible discrepancy remains unknown.

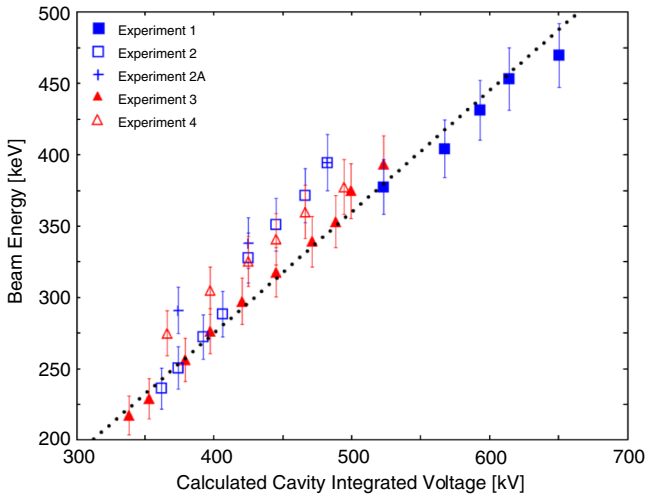

FIG. 17. Beam energy as a function of cavity integrated voltage associated with the fundamental mode, calculated from measurements of the transmitted power, for two cathode locations. Error bars are estimated by summing in quadrature the errors associated with the dipole magnetic field strength and the estimated ±0.5 cm precision of centering the beam centroid on the downstream YAG screen. The trend line slope is 0.85.

6. Beam energy and rf phase

Figure 18 shows the beam energy as a function of rf phase, measured for two cathode locations. During the first test, the procedure was to align the initial beam through the center of the dipole by centering the beam on the first and fourth YAG screens, with the dipole and all intermediate steering and focusing elements degaussed. This alignment was done for a beam with an initial phase of 40 degrees past the zero crossing, 17 pC bunch charge, a laser energy of 84.6 μJ delivered to the cathode, and a transmitted power of −8.1 dBm. The beam was then deflected by the dipole and centered on the first spectrometer line YAG screen to determine the beam energy. The rf phase was adjusted, and the dipole strength was adjusted to keep the beam centered on the spectrometer line YAG screen. This generated the data indicated with open black

TABLE III. Measurements of beam energy vs transmitted rf power.

Experiment	Symbol	Launch phase	Laser energy	Cathode position	Alignment[a]
1	■	50°	154 μJ	−10 mm	. . .[b]
2	□	40°	84.6 μJ	−10 mm	YAG 4, 5 (− 8.1 dBm)
2A	+	40°	84.6 μJ	−10 mm	YAG 4, 5 (− 8.1, −9.2, −10.3 dBm)
3	▲	40°	78 μJ	−8 mm	YAG 4, 5 (− 7.4 dBm)
4	△	40°	103 μJ	−8 mm	YAG 3,5 (− 7.9 dBm)

[a]Indicates location of YAG screens used for alignment, and transmitted power levels at which alignment was performed.
[b]Not recorded.

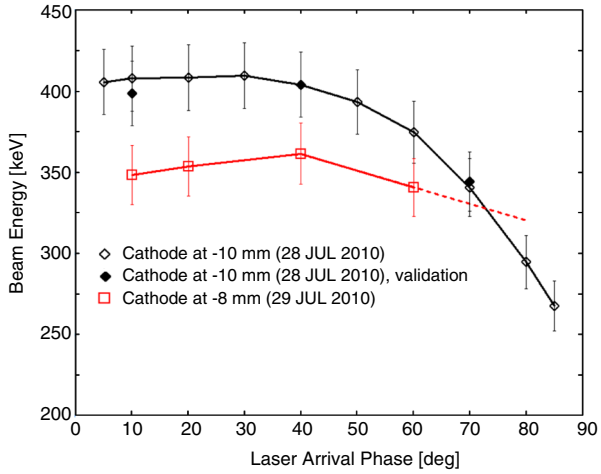

FIG. 18. Beam energy as a function of laser timing, for two cathode locations. Error bars calculated as discussed in the caption for Fig. 17.

diamonds in Fig. 18. This procedure does not guarantee that the beam remained centered in the dipole as the rf phase was varied, so the full alignment procedure was also done before measuring additional points at 10° and 70° phases. These data points (along with the initial 40° data point) are indicated in the figure with solid black diamonds, and suggest that the error due to the procedure used is not too bad. A second experiment was conducted on the following day after moving the cathode from 10 mm retraction to 8 mm retraction. Because of the failure of the fourth YAG screen drive motor, the beam was aligned through the third and fifth YAG screens. As indicated above, this alignment is believed to be worse than was achieved on the previous day using the fourth and fifth YAG screens. Transmitted power was −7.9 dBm, and the laser energy was 103 μJ. Only four data points were taken before the liquid helium supply was exhausted, shown with open red squares in the figure. As no more liquid helium was available during the scheduled experimental run time, it was not possible to perform a revalidation of the data with improved-alignment data as had been done the day before.

Although simulations have not yet been performed of the gun in the operating condition described here, they were performed for the gun at full energy (nominal 1.2 MeV) [24]. These simulations predicted that moving the cathode from 9 mm retraction to 6.5 mm retraction would reduce the beam energy (when operating near the lower cutoff, zero degrees in our notation) by about 50 keV, which is also what we see in our experiment at reduced energy. In addition, the simulations predicted that the curves of beam energy would cross each other near 55 degrees past the zero crossing. Extrapolation of the experimental data for these lower energy tests suggests a crossover near 75 degrees past the zero crossing, as indicated with the dotted line in Fig. 18.

7. Phase scan (beam energy)

To assess the impact of cavity power or nominal beam energy on beam extraction from the gun, a phase scan was performed for beams initially at estimated energies of 300 and 250 keV. The results are shown in Fig. 19. This data was taken at the second diagnostic station and, although uncalibrated, the detector voltage is indicative of bunch charge. The cathode was at 10 mm retraction, and a laser energy of approximately 300 μJ was delivered to the cathode. The data demonstrates a characteristically wide acceptance of launch phases, with the greatest beam transport near the upper phase cutoff. The acceptance window appears to increase as the cavity fields are increased, agreeing with simulations. Note that the beam energies are notional only, since we know from Fig. 18 that the actual beam energy will vary with the launch phase of the electrons.

8. Emittance and intensity

Beam emittance was measured using the slit-screen technique discussed, for example, in Ref. [31]. For these measurements, the first diagnostics module included horizontal and vertical slits of width 0.5 mm, spaced on 3 mm centers, in a 1 mm thick stainless steel plate (Fig. 10). These slits convert the beam into a series of beamlets, which expanded under the influence of the beam's emittance and divergence. These beamlets were then imaged on the YAG screen in the second diagnostics module, 210 mm downstream. Image analysis and calculation of the beam emittance were performed using a LABVIEW program, and sample images used in this process are presented in Fig. 20.

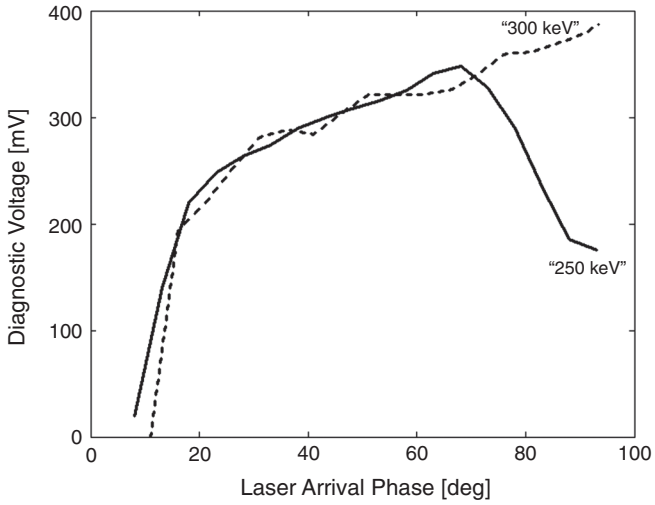

FIG. 19. Diagnostic voltage as a function of laser arrival phase at the cathode, for beams with two nominal energies. The diagnostic was not calibrated during this test, but diagnostic voltage scales with bunch charge. The beam energies are nominal only, since adjusting the launch phase of the electron bunch will affect its energy significantly.

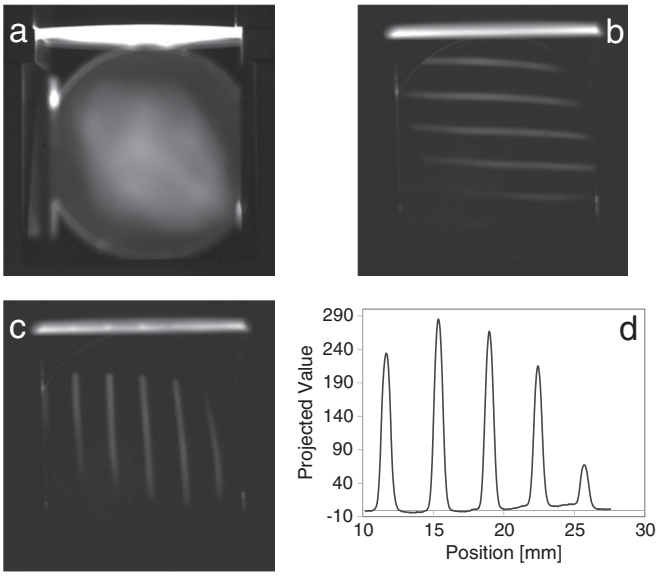

FIG. 20. Images used in emittance measurements, showing (a) YAG screen image of the beam; (b) horizontal and (c) vertical beamlet images; and (d) projected profile for horizontal beamlets. In images (a), (b), and (c), the edge of the YAG screen is visible as a bright rectangle at the top of the image due to guiding of a significant amount of light inside the YAG crystal.

Figure 20(a) shows a YAG screen image of the beam at the first diagnostic station. The horizontal and vertical rms widths of the beam at that location were 3.7 and 3.8 mm, and the beam was diverging rapidly. Figures 20(b) and 20(c) show YAG screen images of horizontal and vertical beamlets arriving at the second diagnostics module. Figure 20(d) shows the projected profile for the horizontal slits, after background subtraction and a small rotation to bring the slit images parallel to the image axis. The projection is done within a rectangular region of interest that is hand-drawn on the image to include the beamlets but exclude any unwanted artifacts. These profiles are used for the emittance calculation, as detailed in the Appendix. The slit spacing of 3 mm is fairly wide, so there are typically only four or five slits across the width of the beam. This small number of slits reduces the accuracy of the measurement, but the wide spacing ensures that beamlets from neighboring slits do not overlap at the viewing screen. Measurements were all nominally performed at the same rf power levels, corresponding to a beam energy of approximately 374 keV. Laser energy and cathode position were varied. Measured normalized rms emittances are listed in Table IV, and averaged 4.9 μm. This beam is highly space charge dominated, as indicated by an intensity parameter [32] value of 0.982, calculated in the Appendix using representative beam quantities.

TABLE IV. Measured normalized rms emittance at 374 keV.

Bunch charge [pC]	Cathode location [mm]	Horizontal emittance [μm]	Vertical emittance [μm]
43[a]	−10	4.9	5.7
41[b]	−10	5.8	5.8
20[b]	−10	4.4	4.2
14[a]	−8	4.0	4.1

[a]Beam energy measured with dipole.
[b]Beam energy estimated from measurement of transmitted power.

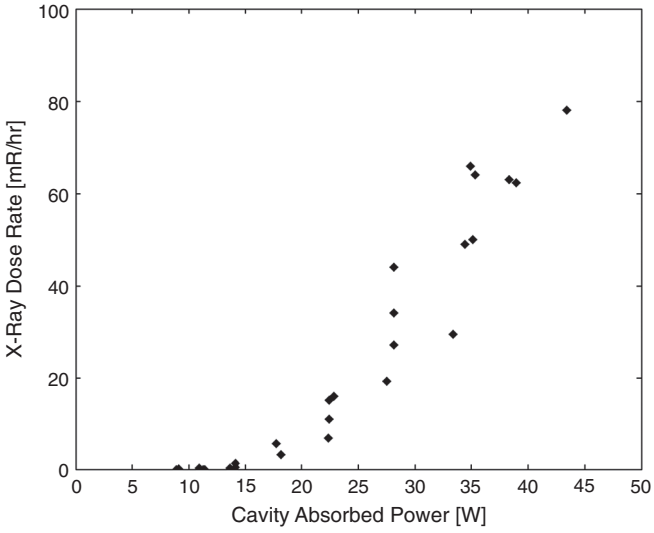

FIG. 21. Radiation dose rate as a function of rf power absorbed in the cavity.

9. Radiation and rf power

Figure 21 shows the radiation dose rate as a function of cavity absorbed rf power, recorded during one series of tests with a radiation area monitor placed close to the cavity. The cathode was at 10 mm retraction and no photoelectron beam was being produced.

IV. SUMMARY

Here, we have reported details of the design and commissioning of the first superconducting quarter-wave resonator electron gun. Although only a prototype, this gun has generally exceeded our expectations and demonstrated remarkably stable, user-friendly operation. A number of potential problems, such as severe multipacting and cavity quenching during operation, have not occurred. Where minor problems have occurred, such as the failure of the NbTi solenoid to superconduct, successful workarounds have been found in short order. Bunch charge and beam energy have reached very respectable levels given that the machine has only been operated as a gun for a total of seven days. No fundamental limits have been reached for either quantity. The measured emittance is satisfactory for FEL operation at the infrared wavelengths planned for the NPS facility.

ACKNOWLEDGMENTS

Funding for this project was provided by grants from the Office of Naval Research and the High Energy Laser Joint Technology Office. The photocathode drive laser was independently procured by Boeing using internal research and development funding. The authors would like to thank Robert Legg for insightful discussions and suggestions.

APPENDIX: EMITTANCE AND INTENSITY PARAMETER CALCULATION

Our calculation of beam emittance from YAG screen images follows the approach of Ref. [31]. Assume a slit-screen system with a slit width of d, a slit spacing of w, and a distance of L between the slits and the screen. Transverse position is denoted by x and the angle with respect to the beam line axis is denoted by x'. For the mth beamlet, we calculate an image intensity

$$I_m = \sum_n Y_n \tag{A1}$$

and the moments

$$\langle x_m \rangle = \frac{\sum_n p_n Y_n}{I_m}, \tag{A2}$$

and

$$\langle x_m^2 \rangle = \frac{\sum_n p_n^2 Y_n}{I_m}. \tag{A3}$$

The index n runs over the pixels in the beamlet, with p_n and Y_n being the position and height of the profile curve at the nth pixel. Once these moments are calculated, the position and angle centroids are removed to obtain centered values of x and x', called $x_{m,c}$and $x'_{m,c}$, according to

$$x_{m,c} = mw - \frac{\sum_m I_m mw}{I_{\text{tot}}} \tag{A4}$$

and

$$x'_{m,c} = \frac{1}{L}\left(\langle x_m \rangle - mw - \frac{\sum_m I_m(\langle x_m \rangle - mw)}{I_{\text{tot}}}\right). \tag{A5}$$

The integrated intensity and the rms width of each beamlet are then calculated using

$$I_{\text{tot}} = \sum_m I_m, \tag{A6}$$

and

$$\sigma'_m = \sqrt{\frac{\langle x_m^2 \rangle}{L^2} - \frac{\langle x_m \rangle^2}{L^2} - \frac{d^2}{12L^2}}. \tag{A7}$$

In Eq. (A7), the square of the rms size of the slit has been subtracted from the square of the rms size of the beamlet so that the resulting value is that from divergence alone and does not include the initial beamlet size. Once these values have been computed for each beamlet, the rms values for the whole beam can be found using

$$\langle x^2 \rangle = \frac{\sum_m I_m (x_{m,c})^2}{I_{\text{tot}}}, \tag{A8}$$

$$\langle x'^2 \rangle = \frac{\sum_m I_m [(x'_{m,c})^2 + (\sigma'_m)^2]}{I_{\text{tot}}}, \tag{A9}$$

and

$$\langle xx' \rangle = \frac{\sum_m I_m x_{m,c} x'_{m,c}}{I_{\text{tot}}}. \tag{A10}$$

Finally, the normalized rms emittance is calculated as

$$\varepsilon_{n,\text{rms}} = \beta\gamma\sqrt{\langle x^2 \rangle \langle x'^2 \rangle - \langle xx' \rangle^2}, \tag{A11}$$

where β and γ are the relativistic factors.

To assess the relative contributions of emittance and space charge in defining the evolution of a beam's envelope, Reiser [32] has defined an intensity parameter χ, which is the ratio of the space charge and focusing terms in the transverse envelope equation of a matched beam. It can also be expressed as

$$\chi = \frac{K}{K + \frac{4}{\beta^2\gamma^2}\frac{\varepsilon_{n,\text{rms}}^2}{x_{\text{rms}}^2}}, \tag{A12}$$

where $K = \frac{2I}{I_0\beta^3\gamma^3}$ is the generalized perveance, I is the beam current, I_0 is 17 kA, $\varepsilon_{n,\text{rms}}$ is the normalized rms emittance, and x_{rms} is the rms beam radius. The parameter varies from 0 to 1, where any value over 0.5 is considered to be "space charge dominated," and any value under 0.5 is considered to be "emittance dominated." Although the diagnostic beam line presently installed on the gun does not provide for matched transport, it is instructive to calculate the intensity parameter that would result from injection into a matched transport lattice. For typical parameters of 374 keV energy, 4.9 μm normalized rms emittance, 30 pC bunch charge, and assuming a 3.7 mm rms radius and a 10 ps pulse length with parabolic line charge density, the peak current in the beam would be 4.5 A, and the corresponding intensity parameter χ would be 0.982. Our system can therefore be considered space charge dominated.

[1] T. C. Katsouleas, R. Alarcon, J. Albertine, I. Ben-Zvi, S. G. Biedron, C. A. Brau, W. B. Colson, R. C. Davidson, P. G. Gaffney, II, L. Merminga, J. D. Miller, B. E. Newnam, P. G. O'Shea, C. K. N. Patel, D. Prosnitz, and E. Zimet, *Scientific Assessment of High-Power*

Free-Electron Laser Technology (National Academies Press, Washington, DC, 2008).

[2] F. Loehl, I. Bazarov, S. Belomestnykh, M. Billing, E. Chojnacki, Z. Conway, J. Dobbins, B. Dunham, R. Erlich, M. Forster, S. M. Gruner, C. Gulliford, G. Hoffstaetter, V. Kostroun, M. Liepe, Y. Li, X. Liu, H. Padamsee, D. Rice, V. Shemelin, E. Smith, K. Smolenski, M. Tigner, V. Veshcherevich, and Z. Zhao, in Proceedings of the 2010 International Particle Accelerator Conference, Kyoto, Japan (2010), p. 45.

[3] A. Michalke, H. Piel, C. K. Sinclair, and P. Michelato, in Proceedings of the 1992 European Particle Accelerator Conference (1992), http://accelconf.web.cern.ch/AccelConf/e92/PDF/EPAC1992_1014.PDF.

[4] D. Janssen, H. Büttig, P. Evtushenko, M. Freitag, F. Gabriel, B. Hartmann, U. Lehnert, P. Michel, K. Möller, T. Quast, B. Reppe, A. Schamlott, Ch. Schneider, R. Schurig, J. Teichert, S. Konstantinov, S. Kruchkov, A. Kudryavtsev, O. Myskin, V. Petrov, A. Tribendis, V. Volkov, W. Sandner, I. Will, A. Matheisen, W. Moeller, M. Pekeler, P. v. Stein, and Ch. Haberstroh, Nucl. Instrum. Methods Phys. Res., Sect. A **507**, 314 (2003).

[5] J. Sekutowicz, in Proceedings of the 2007 Superconducting RF Conference, Beijing, China (2007), p. 424, http://accelconf.web.cern.ch/AccelConf/srf2007/PAPERS/WE306.pdf.

[6] A. Arnold and J. Teichert, in Proceedings of the 2009 Superconducting RF Conference, Berlin, Germany (2009), p. 20, http://accelconf.web.cern.ch/AccelConf/SRF2009/papers/moobau03.pdf.

[7] J. W. Lewellen, H. Bluem, A. Burril, T. L. Grimm, T. Kamps, R. Legg, K. Liu, T. Rao, J. Smedley, J. Teichert, and S. Zhang, in Proceedings of the 2009 Energy Recovery Linac Conference, Ithaca, NY (2009), http://accelconf.web.cern.ch/AccelConf/ERL2009/papers/wg103.pdf.

[8] I. Ben-Zvi and J. M. Brennan, Nucl. Instrum. Methods Phys. Res. **212**, 73 (1983).

[9] D. W. Storm, J. M. Brennan, and I. Ben-Zvi, IEEE Trans. Nucl. Sci. **32**, 3607 (1985).

[10] G. Olry, S. Bousson, T. Junquera, J. Lesrel, G. Martinet, D. Moura, H. Saugnac, P. Szott, P. Bosland, P.-E. Bernaudin, and G. Devanz, in *Proceedings of the 10th European Particle Accelerator Conference, Edinburgh, Scotland, 2006* (EPS-AG, Edinburgh, Scotland, 2006), p. 393.

[11] V. Zvyagintsev, K. Fong, M. Laverty, R. E. Laxdal, A. K. Mitra, T. Ries, and I. Sekachev, in Proceedings of the 10th European Particle Accelerator Conference, Edinburgh, Scotland, 2006 (Ref. [10]), p. 375.

[12] W. Hartung, J. Bierwagen, S. Bricker, C. Compton, T. Grimm, M. Johnson, F. Marti, J. Popielarski, L. Saxton, R. C. York, A. Facco, and E. Zaplatin, in Proceedings of the 2007 Superconducting RF Conference, Beijing, China (2007), p. 296, http://accelconf.web.cern.ch/AccelConf/srf2007/PAPERS/TUP67.pdf.

[13] H. Kabumoto, S. Takeuchi, M. Matsuda, N. Ishizaki, and Y. Otokawa, in Proceedings of the 2009 Superconducting RF Conference, Berlin, Germany (2009), p. 849, http://accelconf.web.cern.ch/AccelConf/SRF2009/papers/typpo093.pdf.

[14] M. P. Kelly, J. D. Fuerst, S. Gerbick, M. Kedzie, K. W. Shepard, G. P. Zinkann, and P. N. Ostroumov, in Proceedings of the 2008 LINAC Conference, Victoria, BC, Canada (2008), p. 836, http://accelconf.web.cern.ch/AccelConf/LINAC08/papers/thp025.pdf.

[15] S. Ghosh, R. Mehta, G. K. Chowdhury, A. Rai, P. Patra, B. K. Sahu, A. Pandey, D. S. Mathuria, J. Chacko, A. Chowdhury, S. Kar, S. Babu, M. Kumar, S. S. K. Sonti, K. K. Mistry, J. Zacharias, P. N. Prakash, T. S. Datta, A. Mandal, D. Kanjilal, and A. Roy, Phys. Rev. ST Accel. Beams **12**, 040101 (2009).

[16] J. W. Lewellen, W. B. Colson, S. P. Niles, W. S. Graves, T. L. Grimm, A. E. Bogle, and T. I. Smith, in Proceedings of the 2008 LINAC Conference, Victoria, BC, Canada (2008), p. 495, http://accelconf.web.cern.ch/AccelConf/LINAC08/papers/tup044.pdf.

[17] S. P. Niles, W. B. Colson, K. L. Ferguson, J. R. Harris, J. W. Lewellen, B. Rusnak, R. Swent, P. R. Cunningham, M. S. Curtin, D. C. Miccolis, D. J. Sox, C. H. Boulware, T. L. Grimm, J. L. Hollister, and T. Smith, in Proceedings of the 2010 Free Electron Laser Conference, Malmö, Sweden (2010), http://accelconf.web.cern.ch/AccelConf/FEL2010/papers/wepb28.pdf.

[18] J. W. Lewellen, W. B. Colson, S. P. Niles, and T. Smith, in Proceedings of the 2008 Free-Electron Laser Conference, Gyeongju, Korea (2008), p. 394, http://accelconf.web.cern.ch/AccelConf/FEL2008/papers/tupph067.pdf.

[19] K. L. Ferguson, C. W. Bennett, W. B. Colson, J. R. Harris, J. W. Lewellen, S. P. Niles, B. Rusnak, R. Swent, and T. Smith, in Proceedings of the 2010 Free-Electron Laser Conference, Malmö, Sweden (2010), http://accelconf.web.cern.ch/AccelConf/FEL2010/papers/mopa04.pdf.

[20] A. W. Chao and M. Tigner, *Handbook of Accelerator Physics and Engineering* (World Scientific, Singapore, 2006), p. 394.

[21] J. C. Jimenez, M. S. thesis, Naval Postgraduate School, 2010.

[22] E. J. Montgomery, J. C. Jimenez, J. R. Harris, D. W. Feldman, P. G. O'Shea, and K. L. Jensen, in Proceedings of the 2010 Free-Electron Laser Conference, Malmö, Sweden (2010), http://accelconf.web.cern.ch/accelconf/FEL2010/papers/wepb12.pdf.

[23] S. H. Hallock, M. S. thesis, Naval Postgraduate School, 2010.

[24] S. P. Niles, Ph.D. dissertation, Naval Postgraduate School, 2010.

[25] H. A. Schwettman, J. P. Turneaure, and R. F. Waites, J. Appl. Phys. **45**, 914 (1974).

[26] C. E. Reece, M. Drury, M. G. Rao, and V. Nguyen-Tuong, in *Proceedings of the Particle Accelerator Conference, Vancouver, BC, Canada, 1997* (IEEE, New York, 1997), p. 3105.

[27] P. L. Anthony, J. R. Delayen, D. Fryberger, W. S. Goree, J. Mammosser, Z. M. Szalata, and J. G. Weisend, II, Nucl. Instrum. Methods Phys. Res., Sect. A **612**, 1 (2009).

[28] J. Knobloch, in *Proceedings of the First International Workshop on Hydrogen in Materials and Vacuum Systems*, AIP Conf. Proc. No. 671 (AIP, New York, 2003), pp. 133–150.

[29] T. Rao, I. Ben-Zvi, H. Hahn, D. Kayran, Y. Zhao, P. Kneisel, and M. Cole, in *Proceedings of the 21st Particle Accelerator Conference, Knoxville, 2005* (IEEE, Piscataway, NJ, 2005), p. 2556.

[30] Q. Zhao, T. Srinivasan-Rao, and M. Cole, in *Proceedings of the 20th Particle Accelerator Conference, Portland, OR, 2003* (IEEE, New York, 2003), p. 2047.
[31] S. G. Anderson, J. B. Rosenzweig, G. P. LeSage, and J. K. Crane, Phys. Rev. ST Accel. Beams **5**, 014201 (2002).
[32] M. Reiser, *Theory and Design of Charged Particle Beams* (Wiley, Weinheim, Germany, 2008), pp. 548–552.
[33] B. Rusnak, ''Navy Shipboard Superconducting Accelerators and Cryogenics,'' Technical Report (2010).